J Mater Sci (2006) 41:5441–5454
DOI 10.1007/s10853-006-0322-2

# Statistical failure analysis of brittle coatings by spherical indentation: theory and experiment

**Rentong Wang · Noriko Katsube · Robert R. Seghi · Stanislav I. Rokhlin**

Received: 19 September 2003 / Accepted: 15 September 2005 / Published online: 13 June 2006


**Abstract** The mode of failure and failure probability of a brittle coating on a compliant substrate subjected to a static load through a spherical indenter is investigated experimentally and theoretically. We extend our recent study (2003, J Mat Sci 38:1589) of surface crack initiation in a monolithic solid to the layered system, and account for the multi axial stress state of the indentation in the failure probability analysis. Two modes of failure, a Hertzian cone crack initiating from the contacting surface and a half-penny-shaped crack initiating from the interface, are investigated and the probability of failure initiation for both surfaces are theoretically predicted and compared with experimental data.The effect of interface debonding on failure phenomena is investigated. For a given load the failure probability for debonded specimens is significantly higher than that of well-bonded samples. For the debonded case the theoretical failure probability curve falls within the 90% confidence interval of the experimental data, while the experimental values for the completely bonded case show somewhat lower failure probabilities than that predicted. This may be attributed to the possible bridging effect by the adhesive on interfacial surface defects in the ceramic that is not accounted for in our model.

R. Wang · N. Katsube (✉)
Department of Mechanical Engineering, Ohio State University, Columbus, OH 43210, USA
e-mail: katsube.1@osu.edu

R. R. Seghi
College of Dentistry, Ohio State University, Columbus, OH 43210, USA

S. I. Rokhlin
Department of Industrial, Welding and Systems Engineering, Ohio State University, Columbus, OH 43210, USA

## Introduction

Layered structures, such as a hard ceramic layer bonded onto a soft substrate, are often used in industrial and military applications to protect substrates from environmental effects (mechanical, thermal, and chemical). The same strategy has been applied to medical implants and various dental restorations such as complete and partial veneering of teeth with ceramics to protect the remaining tooth structure. A more complete understanding of the failure mechanisms of such layered structures is therefore important for damage-tolerant design and further structural improvement.

Indentation testing is the method of choice for characterizing the strength of coated structures and a number of studies [1–4] have been conducted by loading them statically through a spherical indenter. Chai et al. [2] addressed the effect of the interface flaws on fracture of a brittle coating using glass disks bonded to a polycarbonate substrate. In such a system two modes of failure may occur: one initiated from the sample surface, similar to the semispace [5], the other initiated from the bonded interface. They found that when flaws at the interface are removed with etching, cone cracks from the top surface were more likely to occur than half-penny-shaped cracks at the interface. Miranda et al. [3] have further developed a flaw based statistical analysis to account for systematic differences between experimentally observed and theoretically predicted critical loads for the initiation of contact-induced interfacial radial cracks. Tsai et al. [4] addressed the effect of glass-ceramic layer thickness on the surface Hertzian cone crack initiation by a flat indenter loading as well as on crack initiation from the interface. Despite these recent studies, the issue of probability of failure initiation from the contact surface versus the coating/substrate interface has not been fully understood.

In this work, we predict the crack initiation probability for both the contact surface (cone crack) and the interface (half-penny-shaped radial crack). We address this issue both experimentally and theoretically by considering a simple layered structure (Fig. 1) subjected to a static indentation load with different indenter radii. A cone crack is found to initiate from the contact surface for the smaller indenter, while for the larger indenter a half-penny-shaped crack is found to initiate from the interface (bottom surface of the top ceramic layer). We develop a mathematical model to analyze these two distinct modes of crack initiation and the statistical variation of the critical load. We generalize our recent study of surface crack initiation in monolithic solids [5] to the layered structure case and account for the multi-axial stress state of the indentation contact surface in the statistical analysis of failure initiation. We first assume, as Frank and Lawn [6] and Mouginot and Maugis [7] did for a monolithic case, an axi-symmetric cone crack path of $\sigma_3$ trajectory initiating from the top contact surface. The stress intensity factor is then evaluated along the proposed crack path taking into consideration the rapidly changing stress field associated with this contact problem. The variation in crack initiation load is attributed to the flaw size distribution on the specimen surface which is characterized by a fracture-mechanics-based statistical model applicable for a multiaxial stress state. By combining the crack initiation criterion with the flaw size distribution, we predict the probability of cone crack initiation at the top contact surface as a function of load. Statistical parameters related to the flaw distribution were experimentally measured with ball-on-ring flexure tests and the failure initiation probability was evaluated by incorporating the multi-axial stress state of the contact surface. The elastic moduli were measured by ultrasonic methods. These experimentally determined material properties were used in obtaining the theoretical failure probability distributions.

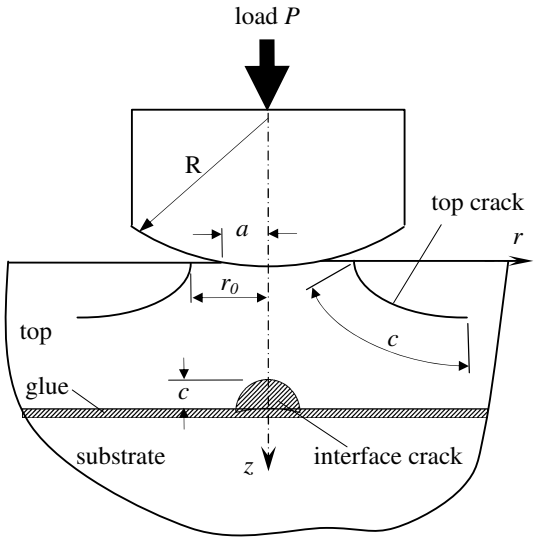


**Fig. 1** Illustration of the two modes of failure: (1) cone crack initiated from the contact surface and (2) vertical half-penny shaped crack initiated from the interface

Since the interfacial region is not in the immediate neighborhood of the contact load, the stress gradient in this region is relatively small and we apply the above-described fracture-mechanics-based statistical multiaxial stress model directly to predict the crack initiation probability at the interface. By comparing the probabilities of the competing mechanisms of crack initiation at the top contact surface and at the interface, we explain the experimentally observed transition of the crack initiation site (contact surface versus interface). We also investigate the effect of the debonding between the coating and the substrate on the critical crack initiation load from the interface by employing indentation tests on a fully debonded model. Theoretical predictions were compared with experimental results.

## Experimental approach

### Materials and sample preparation

Solid borosilicate glass rods (item # 8496K82, McMaster Carr Supplies), 15.9 mm in diameter, were sectioned with a slow speed diamond wheel saw (Leco VC-50, St Joseph, MI) under water coolant into 1 mm thick disks. A total of about 130 disks were fabricated. The surfaces of the glass disks were sanded on a rotating wheel with 600 grit SiC sandpaper under water coolant. The disks were placed in distilled water and cleaned ultrasonically for 5 min prior to examination. The surfaces were examined under a binocular microscope at 15–20× magnification to assure a uniform finish. Any specimen surfaces that showed visible residual saw cuts were marked and re-sanded until a uniform surface finish was observed. The glass disks were randomly divided into three groups.

The ball-on ring biaxial flexure test (Fig. 2) was used to determine the strength of two of the glass disk groups.

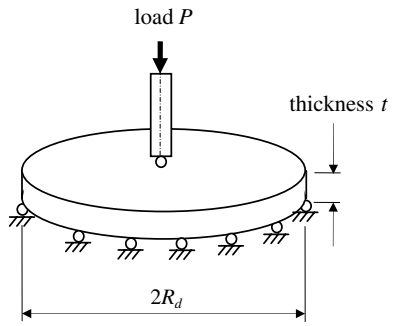


**Fig. 2** Schematic of biaxial flexure test

Approximately one quarter of the disks ($n = 35$) were tested as finished and another quarter of the disks ($n = 35$) were further etched for two minutes with 10% HF acid. The strength data obtained from the biaxial testing were used to determine the surface flaw density distribution of the two different surface conditions.

One surface of each of the remaining disks (third group, $n = 60$) was etched as described above with HF acid. Half of these disks ($n = 30$) were bonded to the composite substrates to make the layered specimens, and the other half ($n = 30$) were simply laid on the composite substrate (nonbonded) to investigate the effect of interfacial debonding.

The composite substrate consisted of continuous-woven glass-fiber-reinforced epoxy resin (Garolite G-10, McMaster Carr Supply). Five millimeter thick parallel sided disks were sectioned from a 15.9 mm diameter solid rod using a standard metal lathe. Both sides of the disks were sanded flat with 600 grit SiC paper prior to bonding. The glass disks were bonded to the composite substrates using standard dental adhesive technology. The bonded surfaces of the glass and composite were treated with a silane coupling agent (Silane Primer, SDS Kerr, Orange CA) and air thinned to form a thin hydrophobic layer. The dental adhesive (Optibond Solo Plus, SDS Kerr, Orange CA) was applied to the silane treated surfaces, air thinned and photopolymerized for 20 s. Finally the two surfaces were cemented together with a dental composite resin cement (Nexus 2, SDS Kerr, Orange, CA) and photopolymerized for 60 s. Any excess resin was removed from the side of the glass with a rubber polishing wheel so that crack initiation observation was possible.

Half of the bonded specimens (15 samples) were vertically loaded using a 1.59 mm spherical radius WC indenter (through standard Hertzian contact), while the other half were indented by a 20 mm spherical radius WC indenter. The non-bonded or debonded specimens ($n = 30$) were indented by a 20 mm radius spherical WC indenter.

## Measurement of elastic properties

The elastic moduli of the borosilicate glass and the composite materials were obtained by ultrasonic measurements of longitudinal $v_{\mathrm{l}} = \sqrt{\frac{\lambda+2\mu}{\rho}}$ and shear $v_{\mathrm{t}} = \sqrt{\frac{\mu}{\rho}}$ wave velocities, where $\lambda$ is Lame's parameter and $\mu$ is the shear modulus. Young's modulus $E$ is $E = \mu(3\lambda + 2\mu)/(\lambda + \mu)$. The density was determined by Archimedes' method. The ultrasonic velocity measurements were performed at 10 MHz by the pulse-echo method using both immersion and contact techniques for longitudinal wave velocity and by the contact method for shear wave velocity. A Panametrics 5073 PR pulser/receiver and a Hewlett Packard 54504-A 400 MHz digital oscilloscope were used for time delay measurements by the signal overlapping technique. The sample thickness was measured by a micrometer. The precision of the measurement is limited by the flatness and parallelness of the sample surfaces and by the couplant effect for the shear wave velocity measurement. We estimate at least three correct digits in the determination of the Young's and shear moduli on our samples. The results are summarized in Table 1.

## Measurement of failure probability distribution of biaxial tests

In this work we have experimentally determined the Weibull parameters of the flaw distribution from the failure probability distribution of the biaxial flexural data [10]. The 1 mm thick glass disks were supported at the edge by a ring of bearings and loaded on the top center through a tungsten carbide (WC) ball indenter with radius of 4.76 mm (Fig. 2). The experiments were carried out on the Universal Testing Machine (Instron Model 4020, Canton, Mass.) at a crosshead speed of 0.01 mm/min. Two groups of specimens were used to obtain the failure probability distribution for both the sanded surface and etched surface conditions. Under this configuration, cracks are initiated from the bottom surface which is subjected to biaxial tensile stress. The fracture initiation loads, $P$, were recorded for each specimen and the data sorted by the magnitude of the failure load. The cumulative probability $F_i$ of crack initiation at the $i$th fracture load $P_i$ was obtained as the median rank [11].

## Measurement of crack initiation in layered structure with different indenter sizes

The bonded layered specimens were loaded with WC indenters having spherical radii of 1.59 and 20.0 mm, and the fully debonded specimens loaded with a 20 mm radius WC indenter. The specimens were vertically loaded on a universal testing machine at a crosshead speed of 0.01 mm/min.

A 20× binocular microscope (SMZ-1, Nikon, USA) was used to observe the crack initiation. The specimens were trans-illuminated from two different directions with fiber optic lights. The microscope was set up to view the specimen through the side of the polished transparent glass disk

**Table 1** Material properties and geometry

| | Top layer | Glue layer | Substrate |
|---|---|---|---|
| Average thickness (mm) | 1.15 | 0.10 | 5.00 |
| Young's modulus $E$ (MPa) | $62.5 \times 10^3$ | $10.21 \times 10^3$ | $12.6 \times 10^3$ |
| Poisson's ratio $\nu$ | 0.19 | 0.33 | 0.35 |
| Fracture toughness $K_{\mathrm{IC}}$ (MPa m$^{1/2}$)[a] | 0.875 | – | – |

[a]Wiederhorn et al. [8, 9]

during the entire test period. The load at which crack initiation was observed was recorded as the initiation failure load. The observed location of crack initiation, either at a contact surface or at an interface, was also recorded. As was done for the biaxial data, the crack initiation loads $P$ were sorted in order of magnitude and the cumulative probability $F_i$ of crack initiation at the $i$th fracture load $P_i$ is obtained as the median rank [11].

## Theoretical analysis

### Probability of crack initiation and growth from the top contact surface

In this section we will develop a method for predicting the probability distribution of crack initiation from the top surface for the model layered structure shown in Fig. 1. The dimensions of this layered structure and the material properties of the individual layers are summarized in Table 1.

#### *Contact pressure distribution for the semispace versus layered case*

The stress field associated with elastic indentation tests on monolithic materials is described by Hertz theory [12]. When friction between the two contact surfaces is ignored the normal contact pressure distribution $p_0$ is given as follows:

$$p_0 = 1.5p_m\sqrt{1-(r/a)^2} \qquad (0 \le r \le a). \tag{1}$$

where $a$ is the contact radius and $p_m$ is the average contact pressure:

$$p_m = \frac{P}{\pi a^2}, \tag{2}$$

$$a^3 = \frac{3PR}{4E*}, \tag{3}$$

where $E^*$ is a reduced elastic modulus

$$\frac{1}{E*} = \frac{1-v^2}{E} + \frac{1-v'^2}{E'}, \tag{4}$$

$R$ is the radius of the spherical indenter; $P$ is the load applied on the indenter; $E$, $v$, and $E'$, $v'$ are the Young's modulus and Poisson's ratio of the top glass layer and those of the indenter, respectively.

The contact pressure distribution for a layered structure subjected to an indentation load is affected by the structure geometry. We have evaluated the distribution by the finite element method using the ABAQUS finite element software package with four-node axisymmetric elements. The spherical indenter is assumed rigid and the special contact elements were employed to numerically handle the contact between the indenter and the top surface of the layered structure.

If the indentation load is sufficiently small and the top layer is sufficiently thick, the presence of the substrate will not affect the contact pressure distribution and in this case, the contact pressure distribution for the layered structure approaches that of the monolithic semispace. To examine whether it is possible to approximate the contact pressure for the layered structure with that for the monolithic material we have compared in Fig. 3 the finite element results for the actual layered structure against the analytical contact pressure distribution for the monolithic material (Eq. 1). The data are for the material and geometrical parameters listed in Table 1; indenter radius is 20.0 mm and load is 500 N. The later is selected since, for the 20 mm radius indenter, the experimentally observed average failure load is around 500 N. In general, the difference between these two curves is not very large. The maximum contact pressure for the layered structure is slightly lower than that for the monolithic material while the contact radius for the layered structure is slightly larger than that for the monolithic material.

The maximum contact pressures and the contact radii normalized to the monolithic case are plotted as a function of applied indenter load in Figs. 4 and 5 respectively for spherical indenters with radii of 1.59 and 20 mm. The two indenter sizes represent the boundaries of the range of indenter sizes used in our experiments. For the small radius indenter, the crack initiation load was experimentally observed to be much smaller than that for the large radius indenter. Therefore, the range of loads used in the simulations for each indenter radius were chosen to be within the range of experimentally observed failure loads. In Fig. 4, the normalized maximum contact pressure is slightly lower than 1.0 while in Fig. 5 the normalized contact radius is slightly larger than 1.0. The plots suggest that the greater the applied load, the more the layered case deviates from the monolithic case. However, the maximum difference

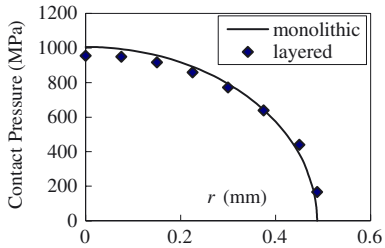


**Fig. 3** Comparison of contact pressure distribution for monolithic and layered cases (500 N load applied by 20 mm radius indenter)

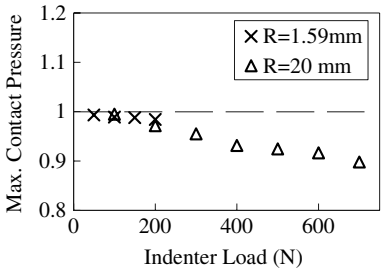


**Fig. 4** Maximum contact pressure for layered structure (Fig. 1) normalized by that for the monolithic case

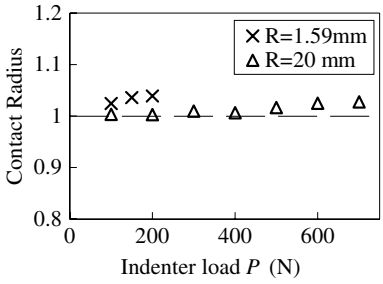


**Fig. 5** Contact radius versus indenter load for layered structure normalized by that for the monolithic case

between the two cases is no greater than 10%. Based on these investigations, it is judged reasonable to approximate the contact pressure distribution for the layered structure by that for the monolithic borosilicate material within the range of parameters used in this study. It is important to note that this approximation holds for the specific layered structure we have investigated. If the thickness of top layer is changed or the material property of the substrate is altered, this approximation may not be valid, and the subsequent analysis based on this approximation may become invalid. Further work is needed to determine the validity of the model as a generalized predictive tool.

*Stress distribution in the top layer*

The thickness of the adhesive layer is much smaller than that of the borosilicate top layer and the elastic properties of the adhesive are very close to those of the substrate (Table 1). For these reasons the effect of the adhesive layer on the stress field inside the top layer and in particular on the contact pressure distribution was shown by finite element calculations to be negligible for the given set of material properties. Therefore, in analyzing the stress field in the vicinity of the contact area on the top surface, the layered structure is approximated by a two-layer structure consisting of a borosilicate top layer perfectly bonded to a composite substrate.

While the finite element method is a powerful tool to evaluate stress distribution, it requires an extremely fine mesh for the rapidly changing stress fields associated with contact problems. However, the applicability to the layered problem of the approximation by the elliptical contact pressure distribution (Eq. 1) makes it possible to readily employ the analytical stress calculation method of Barovich et al. [13] for a perfectly bonded two-layer system (they obtained the exact solution by the Hankel transformation method). In this work their method has been coded and used to evaluate the stress field inside the top layer of borosilicate glass.

To illustrate the effect of a bonded compliant substrate on the stress distribution at the contact surface of the glass, we will again use the case of a 500 N load applied through a 20 mm radius indenter. Figure 6 illustrates the hoop ($\sigma_{tt}$) and radial ($\sigma_{rr}$) stress components on the top surface of the glass as a function of distance $r$ from the center of contact for both the two-layer and monolithic structures. The contact radius $a$ is shown by the vertical dotted line. There were significant similarities between the stress distributions for the two cases. Both stress components are compressive inside the contact area. Outside the contact area, the radial stress component is tensile reaching its maximum value at the edge of the contact area and decreasing monotonically as the distance from the contact edge increases. However, due to the lower modulus of the substrate (see Table 1), the value of the radial tensile stress for the two-layer case is lower at the contact edge and outside the contact area than for the monolithic case.

*Stress intensity factor along the crack path*

For a monolithic semispace, the indenter-induced stress field decreases rapidly with depth ($z$-axis). In order to account for this rapid change in the crack initiation phenomenon, Frank and Lawn [5] have combined the prior stress field (without a crack) and the Griffith energy balance criterion for a crack initiating at the contact edge. Assuming that the crack path is perpendicular to the 1st principal stress $\sigma_1$ and follows the $\sigma_3$ trajectory, they evaluated the stress intensity factor. Mouginot and Maugis [6] further extended the method by Frank and Lawn [5] to include possible crack initiation at various radii $r_0$ outside

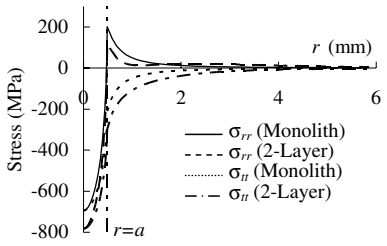


**Fig. 6** Radial ($\sigma_{rr}$) and hoop ($\sigma_{tt}$) stresses on contact surface of glass as a function of radius $r$ (coordinate origin is at the contact area center); vertical line shows contact radius $a$. 500 N load applied through $R$ = 20 mm radius indenter

the contact area. They have also considered the expanding crack front and obtained the stress intensity factor in the form:

$$K_{\mathrm{I}} = \frac{2}{\sqrt{\pi c}} \int_0^c \frac{r_b}{r_c} \frac{\sigma_1(b)}{\sqrt{1 - b^2/c^2}} \, \mathrm{d}(b), \tag{5}$$

where the integral is calculated along the length of the proposed crack path $b$; $c$ is the crack length; $r_b$ and $r_c$ are the radii of the crack at lengths $b$ and $c$; and $\sigma_1$ is the maximum principal stress in the prior stress field.

In this work we have extended the above concept to analyze the contact problem for a layered structure. Employing the assumption of an axisymmetric crack path along the $\sigma_3$-trajectory for the top layer of a layered structure, the effect of the rapidly decreasing stress field $\sigma_1(b)$ on the stress intensity factor along the assumed crack path was evaluated based on Eq. 5. This extension is made possible through the analytical stress representation [13] for a two-layer system. As in the contact problem for the monolithic semispace, the stress intensity factor $K_{\mathrm{I}}$ as a function of crack length $c$ was shown to exhibit a peak indicating possible crack propagation arrest at a crack length above this peak due to a decrease of the stress intensity factor at the crack tip. In contrast to the monolithic case, the crack path for the layered structure is no longer independent of load and the corresponding strain energy release rate can no longer be presented as a non-dimensionalized master curve, as was done in the monolithic case [5]. The analysis for a layered structure, therefore, requires a case-by-case trial and error approach and the details of the analysis are presented by using specific examples.

In Fig. 7, the $\sigma_3$ trajectory of the assumed crack path for the two-layer structure is compared with that for the monolithic case. Both $r$- and $z$- coordinates were normalized by the contact radius $a$. The indenter radius was chosen to be 20 mm and the crack initiation site was chosen to be at $r_0 = 1.15a$ (15% outside the contact edge). For the two-layer structure the $\sigma_3$-trajectory depends on the load level. At a sufficiently small load the contact radius is smaller than the top layer thickness and the $\sigma_3$-trajectory approaches that for the monolithic case. However, with increased load and contact radii, the substrate affects the stress distribution inside the top layer and the $\sigma_3$ trajectory is tilted from that of the monolithic case toward the sample top surface (Fig. 7). The stress component normal to the $\sigma_3$-trajectory (i.e. the maximum principal stress $\sigma_1$) is plotted as a function of crack length in Fig. 8 for the two-layer structure (the graph corresponds to the crack path shown in Fig. 7 for 500 N indentation load). The magnitude of stress rapidly decreases with crack lengths similar to the monolithic case.

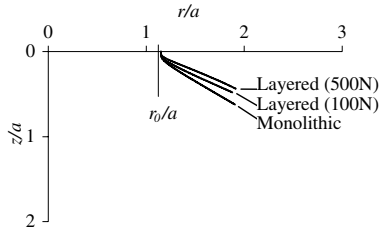


**Fig. 7** Surface crack path normalized by contact radius $a$ in the vicinity of contact area under indentation by 20 mm radius indenter for both layered and monolithic cases. In the monolithic case, the curve is independent of indentation load

*Conditions for crack initiation*

Using the crack path as in Fig. 7 and the stress distribution normal to the crack path, $\sigma_1$, as in Fig. 8, the stress intensity factors for the two-layer structure have been calculated from Eq. 5. They are plotted in Fig. 9 for indenter radius 1.59 mm as a function of crack length for five different indentation loads with a fixed surface radius $r_0 = 1.15a$ of the initiated cone crack. The critical stress intensity factor for borosilicate glass is indicated in the figure by a dashed line. For loads less than 50 N, there will be no crack initiation at radius $r_0 = 1.15a$ regardless of the size of the crack (crack length $c$) because the stress intensity factor along the crack path is always less than the critical value (the minimum critical load for any crack initiating at $r_0 = 1.15a$, therefore, is determined to be

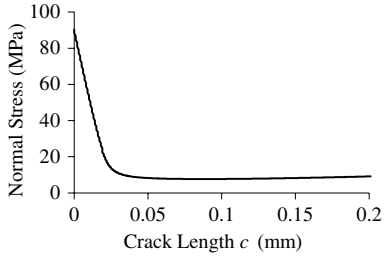


**Fig. 8** Stress normal to crack plane as a function of crack length $c$ for a crack initiated on contact surface at $r_0 = 1.15a$. The crack length is along the crack path shown in Fig. 7 for a layered sample loaded by a 20 mm radius indenter with $P = 500$ N

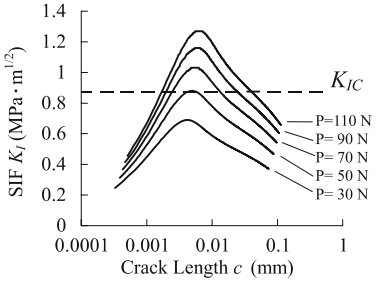


**Fig. 9** Stress intensity factor $K_{\mathrm{I}}$ versus crack length $c$ for crack initiated on the contact surface at $r_0 = 1.15a$ for different loads produced by a 1.59 mm radius indenter

approximately 50 N). As the indentation load increases, the stress intensity factor curve shifts upwards and intersects with the critical stress intensity factor value at two different points. The intersection of the stress intensity factor curves with the critical stress intensity value of the glass will determine the range of crack sizes that have the potential for propagation. If at least one of the preexisting surface defects is equal to or larger than the crack size at the left intersection, it will grow until it reaches such a length that the stress intensity factor is smaller than the critical stress value. From Fig. 9 one determines the load required for crack initiation at $r_0 = 1.15a$.

A multi-site family of curves is shown in Fig. 10 where the stress intensity factor is plotted as a function of crack length for different normalized crack initiation radii ($r_0/a$) for a fixed indenter radius of 1.59 mm and a 70 N indentation load. The critical stress intensity factor is shown by a horizontal dashed line. This graph clearly illustrates the influence of the crack initiation radius on the resulting stress intensity factor curves. For a crack initiation site at $r_0 = 1.7a$, the stress intensity curve is always lower than the critical stress intensity value; therefore, regardless of the crack size, crack propagation will not occur under the given condition. As the crack initiation site becomes closer to the contact area, the stress intensity curves shift upwards and eventually intersect with the critical stress intensity factor line. Again, the values of crack length at the intersection points of the stress intensity factor curve with the critical stress intensity line provide the range of critical crack lengths. It is of interest to point out that the stress intensity curve for a crack initiating right at the edge of the contact area, i.e. $r_0 = 1.0a$, is always below the critical stress intensity factor. This implies that under the given conditions, despite the higher stress concentration on the top surface right at the contact edge (Fig. 6), no crack will initiate and propagate from this site regardless of the crack length. However, for a crack located slightly outside the contact area, $r_0 = 1.1a$ for example, the stress intensity factor curve does intersect the critical stress intensity factor line, and crack propagation becomes possible if a crack with appropriate size preexists at this location.

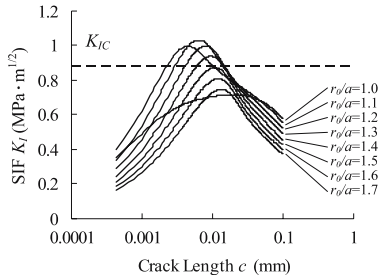


**Fig. 10** Stress intensity factor $K_I$ versus crack length $c$ for crack initiated on the contact surface at different crack initiation radii $r_0$ under 70 N load produced by a 1.59 mm radius indenter

This parametric study shows that the broadest range of preexisting surface critical crack lengths, which propagate at a given indenter load, is at sites slightly outside the contact edge; while preexisting cracks right at the contact edge or far from the contact edge will not propagate under the given conditions. This phenomenon has been observed by numerous investigators under similar experimental conditions [7]. Using a series of stress intensity factor curves, such as those shown in Figs. 9 and 10, and comparing them with the critical stress intensity factor, the minimum critical load for crack initiation can be obtained for a given indenter radius. In the case of the 1.59 mm spherical radius indenter, the critical load is determined from Figs. 9 and 10 to be approximately 50 N.

The above analysis of minimum critical load required to initiate cracks from the contact surface of a layered structure is significantly more complicated than for the monolithic case. In the monolithic case, the strain energy release rate may be represented in a non-dimensionalized form which is independent of load and indenter radius. The envelope of this non-dimensionalized energy release rate as a function of normalized crack length for different normalized starting radii reaches a plateau over a range of flaw sizes and this plateau leads to immediate calculation of the minimum critical load [5, 7]. After appropriate normalization, the stress normal to the crack plane is also independent of load and indenter radius, and thus only a set of master curves for different normalized starting radii is required. This normalization process cannot be applied to the layered case since the stress normal to the crack plane in this case is both load and indenter radius dependent. The addition of a top layer to the contact problem also introduces a scale size (layer thickness) which eliminates the possibility of master curve analysis, and therefore a trial-and-error approach through a series of individual load-dependent analyses is required.

### *Statistical consideration and critical load distribution*

In order to analyze statistical variations of failure associated with the contact problem for a monolithic semispace, Fischer-Cripps [14] combined the Griffith energy balance criterion for crack propagation by Mouginot and Maugis [7] with the well-known Weibull [15] distribution of critical crack sizes. To further employ this concept, Wang et al. [5] experimentally determined the failure load distribution and employed a statistical model of Batdorf et al. [16, 17] to obtain flaw distribution parameters for indentation tests.

In this work the method was further extended to analyze crack initiation and failure phenomena for a layered structure. We also departed from the method of Wang et al. [5] by more accurately reflecting the multi-axial stress state

on the contact surface of a layered model. In particular, the statistical parameters determined by biaxial tests were converted to those for the stress state on the contact surface. According to Batdorf et al. [16, 17], the failure probability caused by surface cracks under a multiaxial stress state can be evaluated by

$$F = 1 - \exp\left[-\int_A \int_0^\infty \frac{\Omega(\sigma, \sigma_c)}{2\pi} \frac{\mathrm{d}N(\sigma_c)}{\mathrm{d}\sigma_c}\, \mathrm{d}\sigma_c\, \mathrm{d}A\right], \tag{6}$$

where $\Omega$ is the solid angle that embeds the crack normals of all cracks of a given size which satisfy the fracture criterion (see Appendix). For a given stress state $\sigma$ we define the critical stress $\sigma_c$, at which a crack with critical length $c^*$ begins to propagate. $N(\sigma_c)$ gives the number of flaws per unit area for which the critical stress varies between zero and $\sigma_c$ ($N(\sigma_c)$ can be interpreted as the crack density function). We will assume that the crack density function $N(\sigma_c)$ takes the following form [18]:

$$N(\sigma_c) = k\sigma_c^m \tag{7}$$

where $k$ and $m$ are the crack density parameters. Equation 7 characterizes the surface roughness associated with a specific surface preparation and the parameters $k$ and $m$ can be determined from experimental strength data such as biaxial and uniaxial tensile tests.

By dividing the top surface area into infinitesimal concentric rings bounded by radii $r^i$ and $r^i + \delta r$ with constant radial stress $\sigma_{rr}$, we rewrite the failure probability for this infinitesimal area as follows.

$$F^i(\sigma_{rr}) = 1 - \exp\left[-(2\pi r^i \delta r)\bar{k}\sigma_{rr}^m\right]. \tag{8}$$

where $\bar{k}$ (Appendix) varies with stress state and is given by

$$\bar{k} = \frac{mk}{2\pi} \int_0^\infty \Omega(\sigma_{tt}\sigma_{rr}, \sigma_c\sigma_{rr}) \cdot \left(\frac{\sigma_c}{\sigma_{rr}}\right)^{m-1} d\left(\frac{\sigma_c}{\sigma_{rr}}\right). \tag{9}$$

Here $\sigma_{tt}$ is the hoop stress and $\Omega(\sigma_{tt}\sigma_{rr}, \sigma_c\sigma_{rr})$ is determined from the actual surface stress state (as shown in Fig. 6) and the fracture-mechanics-based critical stress. In this work, we will employ the fracture criterion where a crack propagates only when the stress normal to the crack plane denoted by $\sigma_n$ reaches the critical stress $\sigma_c$ as follows:

$$\sigma_n = \sigma_c \tag{10}$$

As shown in Fig. 6, a load applied through a spherical indenter to the top surface of the layered structure induces a tensile radial stress $\sigma_{rr}$ and a compressive hoop stress $\sigma_{tt}$ outside the contact area. As a result of this stress state, a crack tends to develop in the hoop direction normal to $\sigma_{rr}$. If the crack is oriented in the $r$-direction, it is subjected to a compressive stress ($\sigma_{tt}$), and may not propagate. The critical range of angles $\Omega(\sigma_{tt}\sigma_{rr}, \sigma_c\sigma_{rr})$ is determined such that the criterion (10) is met for constant $\sigma_{tt}$ and $\sigma_{rr}$ of the given infinitesimal ring area. The physical implication of the new approach represented by Eqs. 8 and 9 is further discussed in the Appendix.

The stress intensity factor of a crack normal to $\sigma_{rr}$ can be approximated as

$$K_\mathrm{I} = \sigma_{rr}\sqrt{\pi c} \tag{11}$$

where $c$ is the length of a crack. Using $K_\mathrm{I} = K_\mathrm{IC}$ in the above equation and Eq. 8, we obtain

$$F^i(c \geq c*) = 1 - \exp\left[-2\pi r^i \delta r \bar{k}\left(\frac{K_\mathrm{IC}}{\sqrt{\pi c*}}\right)^m\right] \tag{12}$$

where $\bar{k}$ is given by Eq. 9, and $c^*$ is a critical crack length for a given stress state and fracture toughness $K_\mathrm{IC}$ Eq. 8 describes the probability of failure as a function of the surface stress state ($\sigma_{rr}$, $\sigma_{tt}$). It does not display any dependence of stress with length; on the contrary, Eq. 12 is recast in terms of the probability of finding a crack with equivalent length equal to or larger than $c^*$. Since the crack density is independent of the nature of the stress state, Eq. 12 holds for all types of actual stress states. The critical crack size $c^*$ in Eq. 12 will be determined by taking into consideration the diminishing stress field with length as discussed in section Stress distribution in the top layer.

The probability of finding at least one preexisting crack with equivalent length between $c_1$ and $c_2$ is given by

$$F_i(c_1 \leq c < c_2) = F^i(c \geq c_1) - F^i(c \geq c_2) \tag{13}$$

Therefore, $F_i$ is the probability of failure with crack initiation within the $i$th annular ring. The failure probability for crack propagation (initiation) from the total top surface area is then given by

$$F = 1 - \prod_{i=1}^{N} (1 - F_i). \tag{14}$$

## Probability analysis of crack initiation from the bonded interface

In this section we will predict the probability distribution of crack initiation and propagation starting from the bonded interface in the brittle top layer of the model two-layer structure. Unlike the cone-shaped crack initiation from the sample contact surface, the crack initiated from

the interface has been characterized as half-penny shape and nearly perpendicular to the interface. This difference in the failure mode is reflected in the analysis. Since the interfacial region is away from the immediate neighborhood of the contact load on the top surface, the change in the local stress distribution along the crack depth ($z$-direction) is relatively mild at the interface. Because of this, the stress intensity factor does not vary significantly along the crack path. The knowledge of a specific flaw distribution and the corresponding critical stress accompanied with the information on the stress distribution at the interface immediately leads to failure probability determination through Eqs. 6, 7 and 10. The details of the stress analysis and the statistical analysis are presented below. The analysis for a completely debonded interface is also included in the discussion. The stress analysis presented in sections Interface Stress distribution for perfectly bonded layers and Effect of interface debonding on interfacial stress distribution was performed by the FEM as described in section Contact pressure distribution for the semispace versus layered case.

*Interface stress distribution for perfectly bonded layers*

The hoop ($\sigma_{tt}$) and radial ($\sigma_{rr}$) stress distribution at the interface between the bonded glass layer and composite are shown as a function of radius $r$ in Fig. 11 for a point and 20 mm radius indenter loads. The stress components were normalized by $P/t^2$, where $P$ and $t$ are the indenter load and the thickness of the top glass layer, respectively. The indentation load of 500 N was chosen as being close to the experimental crack initiation load for the 20 mm radius indenter.

For a point load, the normalized stress distribution is independent of the load. However, due to increases of the contact area with load for the spherical indenter, the stress distribution at the interface varies with the indentation load even after appropriate normalization. When the level of load is so small that the contact area is much smaller than the layer thickness, the normalized stress distribution for the 20 mm radius indenter is almost identical to that of the point load. As the load is increased to 500 N, however, there were significant differences for the stress level at the center between the loading by a point force and a 20 mm radius indenter. In the case of the 20 mm radius indenter, the contact load on the top surface is more widely distributed compared to that of a point load, leading to a significant reduction in the maximum stress components. It is important to note that if the actual contact pressure through a spherical indenter is approximated by a point contact, it will lead to a more conservative estimate of failure load. For an indenter of much smaller radius (1.59 mm), the load required for crack initiation was experimentally determined to be around 200 N. For this level of load, the contact surface radius is very small and the normalized stress distribution at the interface is basically identical to that of the point load distribution shown in Fig. 11. Therefore, for our experimental conditions, Fig. 11 shows the possible maximum differences of stress distributions at the interface.

Figure 12 shows the stress dependence along the central loading axis ($z$-axis) from the contact surface toward the bonded interface in the top glass layer (at $r = 0$ hoop stress $\sigma_{rr}$ and radial stress $\sigma_{tt}$ are equal). An indentation load of 500 N was applied through a 20 mm radius indenter. The compressive stresses directly below the contact point transit to tensile stresses near the bonded interface.

We have observed experimentally that cracks initiating from the interface are generally in planes approximately perpendicular to the bonded surface (Fig. 1). For this reason the crack length is measured in the $z$-axis direction from the interface, and the stress normal to the crack is represented by the hoop stress. In order to examine the stress normal to a crack in the vicinity of the interface, a portion of Fig. 12 is expanded and shown in Fig. 13. It is important to note that the stress normal to the crack plane does not change significantly with the crack depth which is in contrast to the behavior at sample surface (Fig. 8), where the normal stress is shown to decrease very rapidly with the crack length.

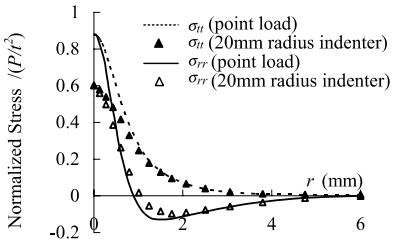


**Fig. 11** Normalized radial ($\sigma_{rr}$) and hoop ($\sigma_{tt}$) stresses on the interface (at bottom surface of the glass) for a three-layer system (Fig. 1). Solid and dashed lines are for a point load (for this case the normalized stress distributions are independent of indenter load); triangle symbols are for the 20 mm radius indenter with 500 N load

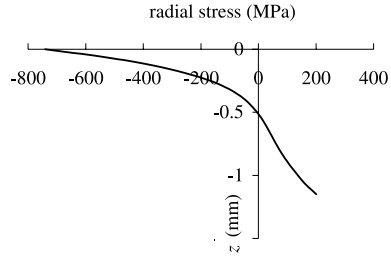


**Fig. 12** Radial stress $\sigma_{rr}$ distribution along $z$-axis from surface toward interface (20 mm radius indenter with 500 N load)

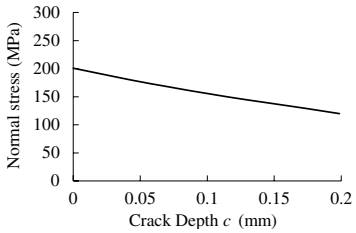


**Fig. 13** Stress normal to crack plane as a function of crack depth $c$ for a crack at the center of and perpendicular to the interface (20 mm radius indenter with 500 N load)

*Effect of interface debonding on interfacial stress distribution*

In section Effect of interface debonding on interfacial stress distribution, the bonding between the top layer and the substrate was assumed to be perfect. However, due to various environmental conditions (both mechanical and chemical) there is a potential for the bond to deteriorate. In actual applications, partial debonding is more likely to occur than total debonding. Even if there was total debonding, there would be friction between the substrate and the top layer. However, in order to illustrate the potential effect of bond deterioration on the failure strength of a layered system, we consider the extreme case of an idealized total debonding without friction. We have compared, in Fig. 14, the stress distributions at the interface as a function of radial distance $r$ from the central loading axis for the perfectly bonded and completely debonded situations. The friction between the top layer and the substrate is assumed to be zero and a point load of 200 N is applied. In both cases, the maximum stress is observed to occur at the $z$-axis ($r = 0$) where the radial and hoop stress components are equal. The maximum interfacial stress resulting from point loading of the debonded top layer is shown to be significantly higher than for an identically loaded bonded layer. This suggests that the critical load for a layered structure is greatly influenced by the bond quality at the interface and bonding deterioration is likely to lead to failure at lower levels of load.

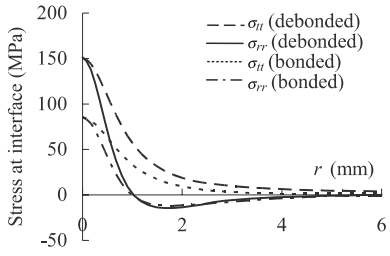


**Fig. 14** Comparison of radial ($\sigma_{rr}$) and hoop ($\sigma_{tt}$) stresses on the bottom surface of the top layer for bonded and debonded cases (200 N point load is applied)

*Probability analysis of interface crack initiation*

To predict the failure probability of a layered structure for both perfectly bonded and completely debonded top layers we will account for the actual stress distribution at the interface and apply Eq. 6 to calculate the statistical failure probability. The flaw density function is again assumed to be in the form (7) with the parameters $k$ and $m$ to be determined experimentally from the biaxial strength tests.

Following the same methodology as in section Conditions for crack initiation, we divide the overall interfacial surface into $N$ infinitesimal concentric ring areas and apply Eqs. 7 and 6 to the $i$th infinitesimal ring area. As shown in Fig. 11, the hoop stress $\sigma_{tt}$ is always larger than the radial stress $\sigma_{rr}$ at the interface which explains why radial shaped cracks are those experimentally observed to initiate at the interface. Therefore, in contrast to Eqs. 8, 9 for the surface crack, the failure probability is expressed in terms of $\sigma_{tt}$ instead of $\sigma_{rr}$ ($\sigma_{tt}$ is normal to the crack plane) and for the infinitesimal ring area is calculated as:

$$F_i(\sigma_{tt}) = 1 - \exp\left[-(2\pi r^i \delta r)\bar{k}\sigma_{tt}^m\right], \tag{15}$$

where

$$\bar{k} = \frac{mk}{2\pi}\int_0^\infty \Omega(\sigma_{\mathrm{rr}}\sigma_{tt}, \sigma_c\sigma_{tt}) \cdot \left(\frac{\sigma_c}{\sigma_{tt}}\right)^{m-1} \mathrm{d}\left(\frac{\sigma_c}{\sigma_{tt}}\right). \tag{16}$$

The overall probability of failure initiation from the interface is obtained by combining the failure initiation probabilities from all infinitesimal ring areas; this is accomplished by inserting Eq. 15 into Eq. 14.

## Comparison of theoretical predictions with experiment

In the data analysis, the parameters describing the surface flaw density functions were determined experimentally by biaxial tests. From these results, the failure probabilities of crack initiation from both the contact and interface surfaces of the glass were predicted for the two spherical indenter sizes. The theoretical predictions were compared against experimental indentation results. In addition, the effect of complete interfacial debonding on the failure probability was predicted theoretically and compared against experimental data.

Determination of flaw distribution parameters

The parameters of the surface flaw density functions were determined by curve fitting of the biaxial test data for both sanded and etched surface conditions. To evaluate the

cumulative probability of fracture for the biaxial tests we will use Eq. 6 by assuming that the crack density function $N(\sigma_c)$ is given by Eq. 7. For the biaxial test data, the cumulative failure probability $F$ is rewritten as

$$F = 1 - \exp\left[-kmR_d^2 I_D \left(\frac{P}{\pi t^2}\right)^m\right], \tag{17}$$

where $I_D$ is given by

$$I_D = \int_0^1 \mathrm{d}\left(\frac{r}{R_d}\right) \int_0^\infty \Omega\left(\frac{r}{R_d}\right) \left(\frac{\sigma_c}{P/\pi t^2}\right)^{m-1} \mathrm{d}\left(\frac{\sigma_c}{P/\pi t^2}\right), \tag{18}$$

where $R_d$ is the plate radius and $t$ is thickness, $\Omega$ (See Appendix) represents the range of critical flaw orientation angles which have been determined from the biaxial stress state and fracture criterion (10). A crack propagates only if its orientation falls within the range of $\Omega$ and the normal stress is larger than or equal to the critical stress $\sigma_c$ according to fracture criterion (10).

The distribution parameters $k$ and $m$ were determined by curve fitting of the experimental data with Eq. 17. Taking advantage of the linearity between $\ln(-\ln(1 - F))$ and $\ln(P)$ a linear regression is employed. Figure 15 presents the experimental data and the best fit obtained by the least squares method. The values of $m$ and $k$ for both sanded and etched surface conditions were determined and the results are summarized in Table 2.

## Analysis of indentation tests

The probability of crack initiation versus failure load obtained from the experimental indentation test using a 1.59 mm radius spherical indenter is represented in Fig. 16 by the open squares. Under these conditions, all failures were initiated from the contact surface. In addition, 90% confidence intervals (dotted lines) are shown based on the 5% and 95% ranks of the experimental data [10]. Using the method described in section Theoretical analysis, the probabilities of crack initiation from both the top surface (dashed line) and the interface (solid line) were calculated

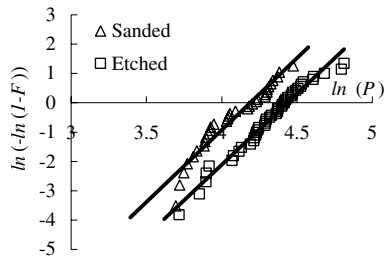


**Fig. 15** Linear regression of transformed biaxial failure load data for sanded and etched surfaces

**Table 2** Flaw distribution parameters

| | $m$ | $K$ |
|---|---|---|
| Sanded surface | 4.917 | $2.361 \times 10^{-11}$ mm$^{-2}$ MPa$^{-4.917}$ |
| Etched surface | 4.852 | $1.873 \times 10^{-11}$ mm$^{-2}$·MPa$^{-4.852}$ |

and are also shown in Fig. 16. The predicted probability of failure from the contact surface is in good agreement with the experimental data. The calculated probability of failure from the interface of the etched glass surface is much smaller than that from the contact surface at a given load. The differences in the two calculated probability curves explain the absence of interface-initiated failures in the experimental data.

Similarly, indentation test results obtained with the 20 mm radius spherical indenter on the layered specimens are shown in Fig. 17. For this large radius indenter, cracks were observed to initiate only from the interface. The model predicts that the failure probability initiating from the contact surface is nearly zero (represented by circles), and the high probability of failure initiation from the interface (solid line) dominates the failure mode at loads greater than about 250 N. The model's prediction of the failure probability from the interface is in good agreement with the experimental data and provides a theoretical basis for the observed differences in failure initiation modes.

The theoretical failure probability distribution curves for the contact surface and those for the interface for a range of indenter radii are presented in Fig. 18. These curves clearly explain why the failure initiation site transits from the contact surface to the interface with increase of indenter diameter. The failure probability of cracks initiating from the contact surface is greatly influenced by the radius of the indenter: the smaller the radius, the lower the critical load. The failure probability of cracks initiating from the interface, however, is minimally affected by the radius of the indenter ranging from

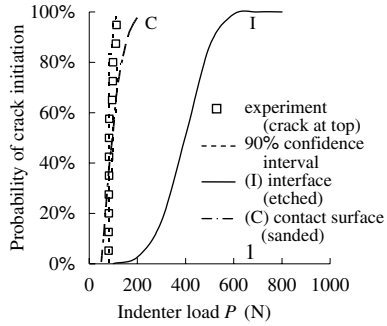


**Fig. 16** Probability of crack initiation versus indentation load. Data for a 1.59 mm spherical radius indenter on a bonded layered sample. Simulated contact surface probability curve is indicated by label ''C'' (broken line) and that for interface by ''I'' (solid line). Experimental results are shown by squares. All cracks were observed to be initiated from the contact surface

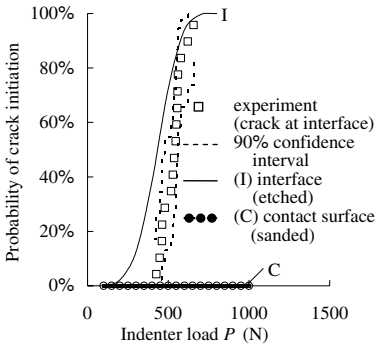


**Fig. 17** Probability of crack initiation versus indentation load for 20 mm spherical radius indenter. Experimental results are shown by squares and simulations by a solid line. All cracks are initiated from the interface

0 mm radius (a point load) to 20 mm radius as shown in the shaded region ''I'' in Fig. 18. This phenomenon is attributed to the small changes in the interfacial stresses generated by indenters of various radii (Fig. 11). It can be observed from the series of probability curves shown in Fig. 18 that for small indenter radii the probability of failure is dominated by cracks initiating from the contact surface while for the larger indenter radii, the half-penny shaped interface-crack initiated failure mode dominates. There exists a range of indenter ball sizes (around 5 mm in radius) where both probabilities overlap and failure may initiate from either the contact or the interfacial surface.

## Effect of interface debonding

The experimental and theoretical failure probability distributions obtained with a 20 mm radius indenter for completely bonded and completely debonded specimens are shown in Fig. 19. For both cases, all failures have occurred from the interface. One can see that the critical loads for the completely bonded case were much higher than those for the fully debonded case. This can be attributed to the higher stress levels that exist on the bottom surface of the fully debonded coating as previously shown in Fig. 14. For the fully debonded case, the theoretical prediction matches the experimental data very well, and it lies within the 90% confidence interval of the experimental data for most of the load range. The theoretical prediction for the completely bonded case, however, results in slightly lower critical loads than the experimental data. Thin films of adhesive, such as those used in our experiments, have been shown to increase the strength of ceramics materials [19]. The increase in strength has been attributed to a crack bridging or healing effect of the surface flaws or a residual surface compressive force caused by the polymerization shrinkage forces in the resin [20]. In either case, our theoretical model did not factor in this effect and the resin strengthening phenomena observed by other investigators may provide some explanation as to why there is a discrepancy between the experimental and theoretical data obtained on the completely bonded specimens.

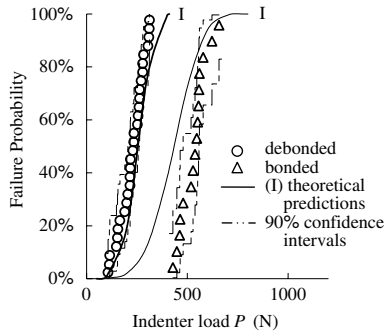


**Fig. 19** Comparison of crack initiation probability from interface for bonded and debonded specimens loaded by a 20 mm radius indenter. Points are experimental, solid lines are predictions

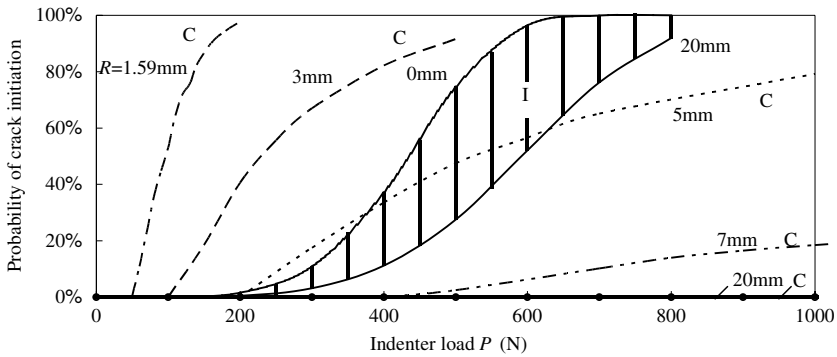


**Fig. 18** Simulated crack initiation probability versus indentation load for different indenter radii (radii of the spherical indenters are shown on the curves). Contact surface probability curves are indicated by ''C''. Interfacial failure probability curves for the range of the used indenter radius are within the shaded area ''I'' ($R = 0$ mm indicates point load). Simulations are for bonded layered sample; all contact surfaces of the glass are sanded, the interfacial surfaces are etched

## Summary and conclusions

The failure of a brittle coating on a compliant substrate (borosilicate glass/cement/composite) subjected to a static load through a spherical indenter was investigated experimentally and theoretically. Two types of failures, a Hertzian cone crack initiating from the contacting surface and a half-penny shaped crack initiating from the interface, were investigated. The statistical failure model for multi-axial stress states developed by Batdorf et al. [16, 17] was employed to characterize the statistical distribution of varying flaw size. These statistical parameters were experimentally determined by biaxial strength tests. With the experimentally measured elastic moduli, these statistical parameters were used in theoretical analysis for predicting failure probability distributions.

In predicting failure probability distributions of cracks initiating from the contact surface, the effect of a rapidly changing stress field associated with an indentation load on the cone crack propagation for a layered system was accounted for analytically. The probability of a cone crack initiation was predicted as a function of indentation load by combining the experimentally obtained statistical distribution of flaws with a fracture-mechanics-based failure criterion. For the contact-surface-initiated cracks in the layered system our analysis is a generalization of the method proposed for a monolithic semispace by Fischer-Cripps [14] and explored by Wang et al. [5]. The statistical model of the failure initiation is further improved by incorporating the multi-axial stress state of the contact surface. In addition, failure probability curves as a function of indentation load were obtained for a half-penny-shaped crack initiation at the interface.

By comparing these two theoretical failure probability distributions, both the crack initiation site (contact surface versus interface) and the failure probability distribution were predicted theoretically. Experimental indentation tests on layered specimens demonstrated that for a small spherical indenter (1.59 mm radius), the failure initiates from the contact surface and the predicted failure probability curve falls within the 90% confidence interval of the experimentally obtained failure probability data for most of the region. For a large spherical indenter (20 mm radius) the failure initiates from the interface as demonstrated by both experimental observations and theoretical predictions. The transition of the mode of failure from surface to interfacial occurs somewhere around a spherical contact radius of 5 mm.

Similar experimental and theoretical investigations were repeated for the complete debonded layered system using the 20 mm radius indenter. In this case all failures were initiated from the interface. Both the experimental and predicted data demonstrated a shift of the failure probability curve towards much lower loads for the fully debonded specimens compared to the completely bonded specimens. The theoretical prediction of the failure probability curve for the debonded specimens fell within the 90% confidence interval of experimental data for most of the region. However, the model predicts somewhat higher failure probabilities than that experimentally obtained for the completely bonded case. This may be attributed to the possible strengthening effect of adhesive on ceramic that is not accounted for in our model.

In many practical applications, loading directions are not necessarily normal to the layer direction. Failure mechanism due to loading parallel to the layered system will need to be investigated in the future in order to address failure probability under general loading conditions.

**Acknowledgments** This research was supported by the Ohio State University Interdisciplinary Biomaterials Seed Grants and by NIHDCR grant number R21 DE014719-02.

## Appendix

### Discussion of statistical parameters for indentation contact problem

In an infinitesimal concentric ring bounded by radii $r^i$ and $r^i + \delta r$ with constant radial stress $\sigma_{rr}$, the failure probability is given [5, 14] as follows:

$$F^i(\sigma_{rr}) = 1 - \exp\left[-(2\pi r^i \delta r) k \sigma_{rr}^m\right] \tag{19}$$

It is implicitly assumed in Eq. 19 that only the maximum principal stress component (must be tensile) affects the failure probability. The influence of the other principal stress components on the failure probability is neglected. For example, in Fig. 20, a crack is oriented in the direction of the principal stress components $\sigma_1$ ($\sigma_1 \geq \sigma_2$). In the case A, the $\sigma_2$ is compressive and in the case B is tensile. Since Eq. 19 does not account for the differences in stress states between A and B (no dependence on $\sigma_2$), the predicted failure distributions of the two cases are identical. Obviously this is not the case. The crack in case A cannot propagate due to compressive stress applied normal to the crack surface, while the crack in case B may propagate if the magnitude of the applied tensile stress $\sigma_2$ satisfies the fracture criterion.

In order to overcome this limitation and more accurately reflect the multi-axial stress states, we will use the method proposed by Batdorf et al. [16, 17] (Eq. 6). Equation 6 accounts for the stress components other than the first principal stress in calculation of the failure probability through the solid angle $\Omega$. Within the framework of the probability model (Eq. 6), the probability of crack

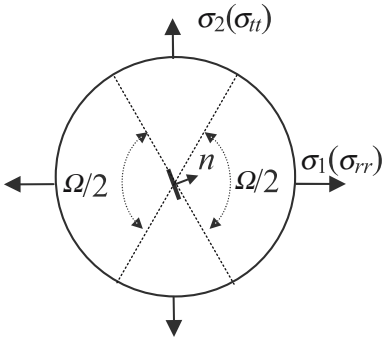


**Fig. 20** Illustration of the two different stress states for a crack. In case A crack is under compression and does not propagate, in case B it propagates while Eq. 19 predicts identical results for both cases

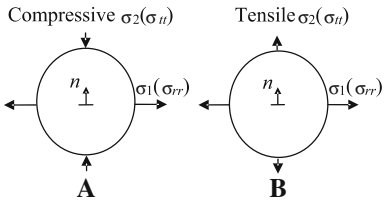


**Fig. 21** Crack under biaxial stress state. Crack propagates when its normal $n$ is in the solid angle $\Omega$

propagation is proportional to $\Omega/2\pi$ and is measured by the probability of its normal $n$ falling within the solid angle $\Omega$. For example in Fig. 21, the failure will occur when the crack normal $n$ is within the sector $\Omega$, and the failure will not occur when $n$ is outside of this sector. Therefore, the influence of $\sigma_2$ on crack propagation probability is accounted for by calculation [16, 17] of the solid angle $\Omega$ for a given stress state (the resulting $\Omega$ will depend on stress state, crack size and failure criterion selected). In particular, if a crack in case Fig. 20B satisfies the failure criterion ($\sigma_2 = \sigma_c$), then $\Omega$ is equal to $2\pi$ and it will propagate, and for the same crack in Fig. 20A, $\Omega$ is less than $2\pi$ and it will not propagate.

To account for the multi-axial stress state, we have derived from Eq. 6 the modified distribution in the form:

$$F^i(\sigma_{rr}) = 1 - \exp\left[-(2\pi r^i \delta r)\bar{k}\sigma_{rr}^m\right], \tag{20}$$

where $\bar{k}$ depends on stress state and is given by

$$\bar{k} = \frac{mk}{2\pi}\int_0^\infty \Omega(\sigma_{tt}\sigma_{rr},\sigma_c\sigma_{rr}) \cdot \left(\frac{\sigma_c}{\sigma_{rr}}\right)^{m-1} \mathrm{d}\left(\frac{\sigma_c}{\sigma_{rr}}\right). \tag{21}$$

Here $\sigma_{tt}$ is the hoop stress and $\Omega(\sigma_{tt}\sigma_{rr},\sigma_c\sigma_{rr})$ is determined from the actual surface stress state.

Equation 20 will reduce to Eq. 19 for a uniaxial tensile stress state.

## References

1. Lawn BR, Deng Y, Miranda P, Pajares A, Chai H, Kim DK (2002) J Mater Res 17(12):3019
2. Chai H, Lawn BR (1999) J Mater Res 14(9):3805
3. Miranda P, Pajares A, Guiberteau F, Cumbrera FL, Lawn BR (2001) Acta Mater 49(18):3719
4. Tsai YL, Petsche PE, Anusavice KJ, Yang MC (1998) Int J Prosthodont 11(1):27
5. Wang R, Katsube N, Seghi RR, Rokhlin SI (2003) J Mater Sci 38:1589
6. Frank FC, Lawn BR (1967) In: Proceedings of the Royal Society of London A299(1458) p 291
7. Mouginot R, Maugis D (1985) J Mater Sci 20:4354
8. Wiederhorn SM (1974) et al ibid. 57:336
9. Wiederhorn SM, et al (1974) In: Bradt RC (ed) Fracture mechanics of ceramics, vol 2, Plenum, p 829
10. Shetty DK, Rosenfield AR, McGuire P, Bansal GK, Duckworth WH (1980) Ceram Bull 59(12):1193
11. Dodson M (1994) In: Weibull analysis. ASQ Quality Press, Milwaukee, Wisconsin. p 66
12. Johnson KL (1996) In: Contact mechanics. Cambridge University Press, Cambridge UK
13. Barovich D, Kingsley SC, Ku TC (1964) Int J Eng Sci 2:253
14. Fisher-Cripps AC (1997) J Mater Sci 32:1277
15. Weibull W (1939) In: A statistical theory of the strength of materials. Handlingar Nr 151. Ingeniors Vetenskaps Akademins, Stockholm
16. Batdorf SB, Crose JG (1974) J Appl Mech 41:459
17. Batdorf SB, Heinisch ML Jr (1978) J Am Ceram Soc 61(7–8):355
18. Chao LY, Shetty DK (1991) J Am Ceram Soc 74(2):333
19. Rosenstiel S, Gupta P, Van Der Sluys R, Zimmerman M (1993) Dent Mater 9:274
20. Burke FJ, Fleming GJ, Nathanson D, Marquis PM (2002) J Adhes Dent Spring 4(1):7